Supplementary Material

Blood Vessel Deformations on Microsecond Time Scales by Ultrasonic Cavitation

Hong Chen, Wayne Kreider, Andrew A. Brayman,
Michael R. Bailey, Thomas J. Matula*

Center for Industrial and Medical Ultrasound, Applied Physics Laboratory,
University of Washington, 1013 NE 40th Street, Seattle, Washington 98105, USA

*To whom correspondence should be addressed; E-mail: matula@apl.washington.edu.

1 Experimental methods

Experiments utilized the injection of microbubbles into the vasculature of *ex vivo* rat mesentery tissue. Compared with rat cecum that was used in the previous report of bubble dynamics observations in *ex vivo* tissues [1], rat mesentery tissue is more optically transparent. The improved transparency enabled clear observation of both the bubble dynamics and the corresponding vessel motions.

1.1 Tissue sample preparation

The protocol used for animal experiments was approved by the Institutional Animal Care and Use Committee (IACUC) at the University of Washington. First, a rat was anesthetized with ketamine and xylazine. Then, the mesentery and intestine were exteriorized through an abdominal midline incision. The exposed tissue was covered with gauze pads moistened with saline solution at 37°C in order to prevent tissue dehydration. The superior mesenteric artery was then cannulated using a 24-gauge angiocatheter. Cannulation was followed immediately by injection of heparinized saline through the catheter to flush out the blood from the mesentery vessels. Next, the portal vein was cannulated by a 20-gauge angiocatheter to serve as an outflow orifice. After the mesentery was clear of blood, the mesentery and intestine were dissected away from the rat body. A vascularized segment of the mesentery was selected and gently spread on a magnetic plate with a semicircular hole (3.5 cm radius) that served as an optical and acoustical window. Then two branches of the superior mesenteric artery and vein feeding the selected mesentery segment were cannulated under a dissection microscope using two polyethylene tubes (outer diameter = 1.64 mm and inner diameter = 0.28 mm). The vasculature of the selected mesentery segment was isolated from surrounding tissue by gently sandwiching the tissue segment between the magnetic plate and an acrylic plate embedded with magnets. The acrylic plate possessed a semicircular hole to match that in the magnetic plate; in addition, it possessed a small opening for the two polyethylene tubes. The mesentery segment was thus sandwiched between the two annular plates (see Fig. S1b).

During these preceding steps, care was taken to spread the mesentery to its natural length without overstretching it. Then, microbubbles mixed with green India ink and saline were injected using a syringe pump into the selected mesentery segment though one of the tubes, with the other tube acting as an outflow vent. In this way, microbubbles could only be injected into the targeted mesentery segment. The microbubbles we used were a commercially available ultrasound contrast agent (Definity®) with a mean diameter from 1.1 μm to 3.3 μm and a maximum diameter of 20 μm. A highly diluted suspension of microbubbles was used to improve the chances for single-bubble events within the observation field. The green India ink was used to increase the optical contrast of the vessels relative to surrounding tissues and also to indicate blood vessel leakage. Tissue preparation was completed within 1 hour and data were collected within the following three hours.

1.2 Equipment and settings

The prepared mesentery tissue sample was transferred to an acrylic tank filled with phosphate buffered saline solution and located on the stage of an inverted microscope (TE2000-U; Nikon Inc., Melville, NY, USA). For microscopic imaging, both a 40× water-immersion objective (numerical aperture 0.8; nominal working distance 3.5 mm; nominal depth of field 0.43 μm) and a 60× water-immersion objective (numerical aperture 1.0; nominal working distance 2 mm; nominal depth of field 0.28 μm) were used. The microscope was aligned confocally with a focused ultrasound transducer (H102; Sonic Concepts, Bothell, WA, USA) with a center frequency of 1 MHz, a geometrical focal length of 63 mm and an f-number of 0.9. The transducer was driven by a single cycle of a sine wave produced by a function generator (33120A; Hewlett Packard, Palo Alto, CA, USA) and amplified by a power amplifier (ENI A150; ENI, Rochester, NY, USA). Because of the ringing of the transducer, the acoustic pulse was about 2 cycles long as determined with a fiber-optic hydrophone (FOPH 2000; RP Acoustics, Leutenbach, Germany). A high-speed camera (Imacon 200; DRS Hadland, Cupertino, CA, USA) was connected to the microscope and synchronized with the transducer. When microbubbles were found in the field of view of the microscope, a single ultrasound pulse was generated and the camera was triggered to capture a 14-frame sequence of images. The exposure time for each frame was 50 ns, while the interframe time was 300 ns. The entire recording time of the camera was about 4 μs, which lasted longer than the ~2 μs ultrasound pulse. Over this time, illumination was provided by a high-intensity, point-source flash lamp coupled to an optical fiber. See Fig. S1a for a schematic of the experimental arrangement.

1.3 Discussion of test conditions

Fiber optic hydrophone measurements were used to characterize the acoustic field produced by the transducer under two conditions: (1) free-field conditions that excluded the water cone, the optical illumination fiber, and the microscope objective; and (2) *in situ* conditions as depicted in Fig. S1a, for which the tissue was removed during measurements. Comparing measurements from these conditions across a range of transducer output levels, we conclude that peak negative pressures were reduced in magnitude by about 9% in the presence of the water cone, illumination fiber, and objective. Unless noted otherwise, reported pressures reflect *in situ* test conditions.

As shown in Fig. S1a, the microscope objective was relatively close to the tissue under observation; accordingly, the potential for the objective to affect the acoustic field at the target site was assessed using *in situ* hydrophone measurements. As plotted in Fig. S1c, each acoustic pulse initially reached the hydrophone at 0 μs, after which it traveled to the objective and was reflected back to the hydrophone. For the 40× objective, the time delay of the reflected wave was 4.3 μs, which was longer than the duration spanned by the captured image frames. As such, the presence of the 40× objective did not affect observed bubble-vessel interactions. For the 60× objective, the delay of 2.6 μs was shorter than the time span of captured images, though the reflected wave did not overlap the primary pulse. Of the data presented here, only three bubble-vessel interactions utilized the 60× objective (including sequences c and d from Fig. 3). These interactions exhibited the same qualitative behaviors as those using the 40× objective, likely because the largest portion of the reflected pulse arrived near the end of the high-speed imaging and was much smaller than the primary pulse. The proximity of the 60× objective does not appear to have altered the basic mechanics of the observed bubble-vessel interactions.

Another relevant aspect of the experimental arrangement was the thickness of the tissue samples. Because rat mesentery is thin, it is almost optically transparent and provides a useful and convenient model for direct observations of bubble-vessel interactions. Whether or not it also represents adequately more three dimensional tissues is addressed here. The thicknesses of several mesentery tissue samples were measured based on histology sections. For these samples, the mesentery thickness was typically more than 1.5 times the diameter of the target vessel within the sample. As noted in the Results section of the main text as well as in other work [2], tissue viscosity may play a significant role in bubble-vessel interactions. To evaluate how the limited thickness of tissue surrounding the vessel might have affected observations, we consider the observed bubble motions along with associated viscous dissipation. For spherically symmetric fluid motion, the rate of viscous energy dissipation per unit volume in an incompressible fluid can be expressed as $2\eta\left[(\partial u/\partial r)^2 + 2(u/r)^2\right]$, where u is the radial velocity, r is the radial coordinate, and η is viscosity [3]. Assuming that tissue is 100 times more viscous than water [2], this expression can be used to estimate the fraction of viscous dissipation that occurred for a tissue sample in water relative to the amount that would have occurred in unbounded tissue. To perform such a calculation, two simplifying assumptions are convenient: first, the bubble, vessel, and surrounding tissue are taken to be spherically symmetric; second, differences in the acoustic impedances of tissue and water are neglected so that no reflections occur and the velocity field everywhere around the bubble can be calculated readily. For an incompressible fluid, the radial velocity field can be expressed as $\dot{R}(R/r)^2$, where R is the bubble radius and the overdot indicates a time derivative. Integrating the viscous dissipation function in space and in time, total energy dissipated can be calculated. We note that viscous dissipation in water is not important (both inside the vessel and beyond the tissue sample) under such conditions. For tissue thickness T and vessel diameter D, the fraction of energy dissipated in a tissue sample relative to that in unbounded tissue is approximately $1 - (D/T)^3$. Thus, even for $T/D = 1.5$, about 70% of a 'maximal' amount of viscous dissipation would be captured by the finite tissue sample. This result suggests that the mesentery tissue samples are thick enough to serve as an effective model for vessels surrounded to greater depths by viscous tissue; *i.e.*, it is a reasonable physical model for more fully three dimensional tissues.

Lastly, we consider the impact of saline in vessels rather than blood. Although blood is several times more viscous than saline, the present study involved acoustic excitation amplitudes at which the resulting bubble dynamics were controlled by the inertia of the surrounding medium rather than its viscosity (see the radius-time curves from Fig. S2). This point can be made more formally by considering the Reynolds number of the flow around the bubble. For a bubble collapsing near a boundary, Popinet and Zaleski [4] defined the Reynolds number as $\rho u R/\mu$, where ρ is the liquid density, μ is the liquid viscosity, $u = \sqrt{p_\infty/\rho}$ is a characteristic velocity, and R is the bubble radius. Since they studied the unforced collapse of laser-generated bubbles, p_∞ was the atmospheric pressure and R was the initial radius prior to collapse. For the present conditions, we define p_∞ as the peak negative pressure and R as the corresponding maximum bubble radius prior to collapse. For the lowest-amplitude pulse of 0.8 MPa considered in this work, the maximum bubble radius can be estimated roughly as 10 μm. Assuming a liquid density of 1000 kg/m^3 and a viscosity of 0.005 Pa·s (five times larger than that for water), we then calculate a Reynolds number greater than 50 for the ensuing collapse. Popinet and Zaleski defined flow regimes identified by low, medium, and high Reynolds numbers. They consider Reynolds numbers below about 20 to belong to the 'low' regime, while Reynolds numbers above about 30 to belong to the 'high' regime. Hence, even our conservative estimate of a Reynolds number of 50 for bubbles in blood would be well into the "high" regime, such that inertial forces significantly exceed viscous forces in characterizing the collapse dynamics. Accordingly, it is unlikely that the presence of saline rather than blood significantly affected test conditions.

1.4 Image analysis

For each ultrasound pulse, the high-speed camera was triggered to capture 14 sequential images. Images were modified in Adobe Photoshop (Adobe Photoshop CS4 11.0; Adobe Systems Inc, San Jose, CA) to adjust only the gray level, brightness, and contrast of the entire image. For presentation purposes, only particular frames that highlight bubble and vessel responses are displayed. Images were calibrated against a stage micrometer with 10 μm per division. Using ImageJ software (ImageJ 1.41o; National Institutes of Health, Bethesda, MD, USA), the scale of the high-speed images was determined to be 9.4 pixels/μm for the 60× objective and 6.3 pixels/μm for the 40× objective.

In preparation of Figs. 2 and 4, vessel-wall positions were identified and displacements were measured relative to the identified position from the first frame of a given sequence (displacements toward the lumen were defined to be negative). While Fig. 2 shows diametral displacements and Fig. 4 shows radial displacements, the same steps in MATLAB (Matlab R2007b; Mathworks Inc., Natick, MA, USA) were taken to identify the relevant vessel-wall locations:

a) A line determining the orientation of the vessel's axis was defined by user selection.

b) A point was selected by the user to define the center of the bubble. The same location was used for all image frames.

c) Aided by a guideline drawn through the center of the bubble and perpendicular to the vessel axis, the user identified the point on the vessel wall that intersected with the guideline. This point defined the measured vessel wall position.

Each of the above steps inherently involves user-to-user variability. To assess such measurement uncertainties, four independent observers defined vessel-wall locations for all of the frames from sequences a–d in Fig. 2. Inter-observer variability in displacement measurements was less than 1 μm for most of the frames; however, higher variability (between 1 and 2 μm) occurred in about 10% of the frames for which the vessel boundary was especially ambiguous. Additional measurement uncertainties of about 1 μm were also present, owing to the frame-to-frame alignment jitter of the camera's optics. For image sequences a–d, we estimate that uncertainties in displacement measurements ranged from 1–3 μm.

In order to directly compare the displacement measurements as plotted in Fig. 3, a common temporal axis was adopted. Although the experimental setup enabled consistent triggering of the camera and the ultrasound transducer, some variability in the positioning of the tissue sample was unavoidable. Such positioning uncertainties led to uncertainties in the timing of image frames relative to the arrival of the ultrasound pulse. For example, a timing uncertainty equivalent to the interframe time of 300 ns would be caused by a positioning uncertainty of about 0.5 mm. To reduce this timing variability, we note that the first bubble collapse usually occurred about 1 μs after arrival of the start of the ultrasound pulse. This observation held across a wide range of pulse amplitudes and vessel sizes and was confirmed independently by simulating the dynamics of a free-field gas bubble exposed to the measured ultrasound pulses. Accordingly, a common temporal axis was adopted for all photographic observations by assigning a time of 1 μs to the frame corresponding to the first bubble collapse.

In addition to vessel-wall positions, bubble radii were also measured from images as shown in Fig. S2. Within each image frame, the bubble was assumed to be ellipsoidal in order to estimate its volume. This volume was then interpreted in terms of an equivalent radius for a spherical bubble. Major and minor ellipsoidal dimensions were estimated interactively in MATLAB by two simultaneous users.

2 Discussion

With regard to the observed vessel motions, it is insightful to consider the time scale in the context of forced mechanical responses versus evoked biological responses. As noted in the main text, Fig. 4 shows that vessel walls moved inward at a speed of around 9 m/s over a time duration of about 1 μs. Could this wall motion be an evoked rather than a forced response? The answer is 'no'. While nerve conduction speeds are fast (~50 m/s), the maximum cycle frequency for individual nerve cell depolarization and repolarization is around 500–1,000 Hz, corresponding to periods of 1,000–2,000 μs [5]. Similarly, a typical skeletal muscle motor unit action potential period is of order 30,000 μs [6]. Even in the hummingbird, in which wingbeat frequencies are ~35–45 Hz, the period for pectoral muscle contraction is ~8,000 μs [7]. However, the asynchronous flight muscles of insects can produce even faster wingbeat frequencies [8], with an apparent 'record' maximum of around 1,000 Hz [9], indicating that antagonistic flight muscles can contract with a period of 500 μs. Mandible closure in the trap-jaw ant *Odontomachus bauri* is muscle-driven and is extremely fast (closing speeds are ~40 m/s; closure occurs in about 100 μs); however, the process relies on the triggered release of energy stored in pre-tensioned muscles rather than on nerve-stimulated muscle contraction [10]. In any case, all of these biological response times are two to five orders of magnitude greater than the entire period of observation illustrated in Fig. 4. Indeed, the fastest 'biological' response time of which we are aware—and which, at a 2 μs period is comparable to the blood vessel wall response times observed here—is molecular: the enzyme carbonic anhydrase, when fully saturated with substrate, operates at ~0.6 MHz [11].

Compare the timing of the bubble motions (Fig. S2) with the vessel response (Fig. 4), it is evident that vessel deformations lagged the incident acoustic pressures and the corresponding bubble responses. Indeed, the maximum invaginations occurred after vessel motions had largely stopped (especially in sequences **a** and **c**). Vessel deformations after the final image frame at 3.9 μs were further explored by delaying some image frames. From these observations, vessels recovered their initial shapes on a time scale of milliseconds (Fig. S3). The time dependence of vessel deformations demontsrate that vessels and surrounding tissues exhibited both viscous and elastic properties.

3 Bernoulli analysis of confinement effects

As an initial step in understanding how bubbles and vessels interact, we can consider the pressure field around an oscillating bubble. If the radial bubble dynamics are presumed, then the estimated pressures around the bubble can be taken as a 'forcing' for an adjacent vessel. Obviously, this simplified approach neglects the coupling between bubble and vessel motions; however, because we have direct observations of bubble motions in vessels, such a phenomenological approach may yield insight into how such bubble dynamics can lead to preferential vessel invagination. By enforcing the conservation of mass and momentum in a liquid, a well known Bernoulli-type equation can be derived for pressures attributable to flow around a bubble [12]. To gain insight into experimental observations, we modify this equation based on geometrical flow considerations.

To explore the geometric confinement of flow between a bubble and a nearby boundary, we consider a bubble oscillating near a flat boundary as illustrated schematically in Fig. S4. First, we assume that the flow remains cylindrically radial near the gap δ. Then, the key assumption is that the bubble's instantaneous rate of volumetric change is directly proportional to the flow rate into the gap δ. Because the volumetric change and the gap distance δ are known *a priori* from the radial bubble dynamics, pressures can be calculated directly for this confined, locally cylindrical (CYL) flow geometry. This formulation is described in more detail below. For comparison, the well known formulation for the classical case of unconfined, spherical (SPH) flow is also described. The Bernoulli analysis below parallels that presented at the 2009 International Ultrasonics Symposium [13]. To define notation, conservation of mass and momentum in an incompressible, inviscid liquid can be expressed as

$$\nabla \cdot \mathbf{u} = 0 \tag{S1}$$

$$\frac{\partial \mathbf{u}}{\partial t} + \mathbf{u} \cdot \nabla \mathbf{u} = -\frac{1}{\rho} \nabla p \tag{S2}$$

where $\mathbf{u}$ is the velocity vector, ρ is density, and p is pressure.

3.1 Spherical flow

Under conditions of fully spherical flow, we integrate Eq. (S1) radially from the coordinate r to the bubble radius R to determine the spatial variation of velocity:

$$u_r = u_R \left(\frac{R}{r}\right)^2 . \tag{S3}$$

Here, u_r is the radial velocity at an arbitrary radial position r and $u_R = \dot{R}$ is the radial velocity at the bubble wall (note that the overdot indicates a time derivative). Then, we consider the boundary conditions $u_r(r = \infty, t) = 0$ and $p(r = \infty, t) = p_\infty$ and integrate the radial component of Eq. (S2) to obtain

$$\int_\infty^r \frac{\partial u_r}{\partial t}\, dr + \frac{1}{2} u_r^2 = -\frac{\Delta p}{\rho} \tag{S4}$$

where $\Delta p = p(r, t) - p_\infty$ represents the pressure change induced by the bubble. Substituting Eq. (S3) into (S4), the pressure Δp is given by Eq. (1) in the main text and is repeated here:

$$\frac{\Delta p}{\rho} = \left(R\ddot{R} + 2\dot{R}^2\right) \frac{R}{r} - \left(\frac{1}{2}\dot{R}^2\right) \frac{R^4}{r^4} . \tag{S5}$$

For comparison with the confined geometry described below, Eq. (S5) can be evaluated at $r = R + \delta$ to calculate Δp at a location corresponding to the nearest point on the boundary depicted in Fig. S4.

3.2 Locally cylindrical flow

For confined flow, we model the locally cylindrical geometry illustrated in Fig. S4 by making a simple observation about the volumetric flow rate between the bubble and the boundary. We note that as the bubble volume changes, a fraction of this volume change must be accommodated by an equivalent volumetric flow of liquid into the gap δ. Assuming a uniform radial flow into the gap δ, we estimate the radial flow velocity at the bubble's instantaneous radius R by equating the rate of volume change of the upper half of the bubble $[\frac{1}{2}(4\pi R^2 \dot{R})]$ with the flow rate across the cylindrical surface defined by R and δ. As such, the flow velocity at $r_c = R$ can be calculated:

$$u_R = \frac{R\dot{R}}{\delta} \, . \tag{S6}$$

Note that the radial coordinate r_c is cylindrical and distinct from the spherical radial coordinate r. Although we could reasonably define the model using a flow rate derived from some other fraction of the bubble's volume change, the model results would be qualitatively similar. Given that Eq. (S6) pertains only to flow between the bubble and the boundary, we recognize it as describing a type of near-field confinement.

To continue the derivation, we consider the continuity equation (S1) in order to ascertain the flow field elsewhere. Still assuming cylindrical axisymmetry, we integrate from an arbitrary radial location r_c to the bubble radius R to obtain

$$u_{rc} = u_R \left(\frac{R}{r_c}\right)^{\alpha} \tag{S7}$$

where $\alpha = 1$ and u_R is given by Eq. (S6). For the case at hand, we model the flow as *locally* cylindrical near the bubble and the boundary; however, there is no reason to expect all flow to remain parallel to the boundary away from the bubble. Instead, we assume that the flow streamlines diverge spherically far from the bubble and take $\alpha = 2$, which enables comparison with fully spherical flow by isolating the impact of near-field confinement. However, we also recognize that adopting a value of α less than two would simulate a type of far-field confinement that is relevant to bubbles in vessels.

For a streamline that remains both close and parallel to the boundary, fluid velocity remains cylindrically radial far from the bubble and the momentum equation (S2) simplifies to a single scalar equation in the radial direction. Considering boundary conditions analogous to the spherical case, we integrate along this streamline:

$$\int_{\infty}^{r_c} \frac{\partial u_{rc}}{\partial t} \, dr_c + \frac{1}{2} u_{rc}^2 = -\frac{\Delta p}{\rho} \, . \tag{S8}$$

Inserting Eqs. (S6) and (S7) into (S8), we express the pressure as follows:

$$\frac{\Delta p}{\rho} = \left(\frac{R^2 \ddot{R}}{\delta} + \frac{3R\dot{R}^2}{\delta} + \frac{R^2 \dot{R}^2}{\delta^2} \right) \frac{R}{r_c} - \left(\frac{R^2 \dot{R}^2}{2\delta^2} \right) \frac{R^4}{r_c^4} \, . \tag{S9}$$

Note that we have assumed a constant standoff distance between the center of the bubble and the boundary so that $\dot{\delta} = -\dot{R}$. Given the nature of the approximation, this relation for Δp is applicable across the gap δ

and at the surface of the boundary. Because no attempt has been made to describe the flow for $r_c < R$, the pressure at any given time for interior radii is assumed to be equal to the value at $r_c = R$.

To compare spherical and locally cylindrical flows for assessment of the influence of near-field confinement, we evaluate pressures at the location corresponding to the point along the boundary that is closest to the bubble. More specifically, Eq. (S5) for spherical flow (SPH) is evaluated at $r = R + \delta$ while Eq. (S9) for locally cylindrical flow (CYL) is evaluated at $r_c = R$. For both geometries, when the bubble reaches its maximum radius so that $\dot{R}$ vanishes and $\ddot{R}$ is negative, the confinement should be strongest while Δp is negative. Moreover, at this instant, the near-field confinement for the locally cylindrical geometry is captured by a pressure scaling factor that is inversely proportional to the gap width [*i.e.*, CYL $=$ SPH $\times$ $(R + \delta)/\delta$]. This scaling demonstrates that negative pressures at the boundary are expected to become arbitrarily large as the bubble approaches the boundary and $\delta \to 0$. Such a near-field confinement effect is shown by the calculation results plotted in Fig. S5a. In addition, calculations are presented in Fig. S5b to explore far-field confinement characterized by $\alpha < 2$.

3.3 Discussion of bubble asymmetry

Assuming bubble sphericity in the vicinity of a boundary at first seems questionable. A bubble collapsing near a rigid boundary will translate toward the boundary and/or form a liquid jet directed toward the boundary [14, 15]. As such, we would expect the bubble's radial velocities to be asymmetric and smaller in magnitude on the side nearest to the boundary. Thus, an assumption of sphericity would overestimate any effects of flow confinement on the flow velocity u_R near the boundary and into the gap δ. However, our observations are not consistent with the vessel wall behaving as a rigid boundary. Rather, we observed bubble translation and/or jetting to be directed *away* from the nearest vessel wall so that flow accelerations and velocities would be greatest on the boundary side of the bubble during collapse. As discussed by Brujan et al. [14], such behavior can occur if energy is stored in the boundary's distention during bubble growth and then re-introduced into the flow during collapse. Although such a complicated interaction is not modeled here, the model presented above elucidates how asymmetric flow associated with jetting away from a boundary can strenghten near-field confinement effects that include a bias toward negative pressures. The assumption of spherical symmetry makes the problem tractable within our phenomenological approach and likely provides a conservative estimate of the effects of near-field confinement in vessels.

4 Supplementary Figures

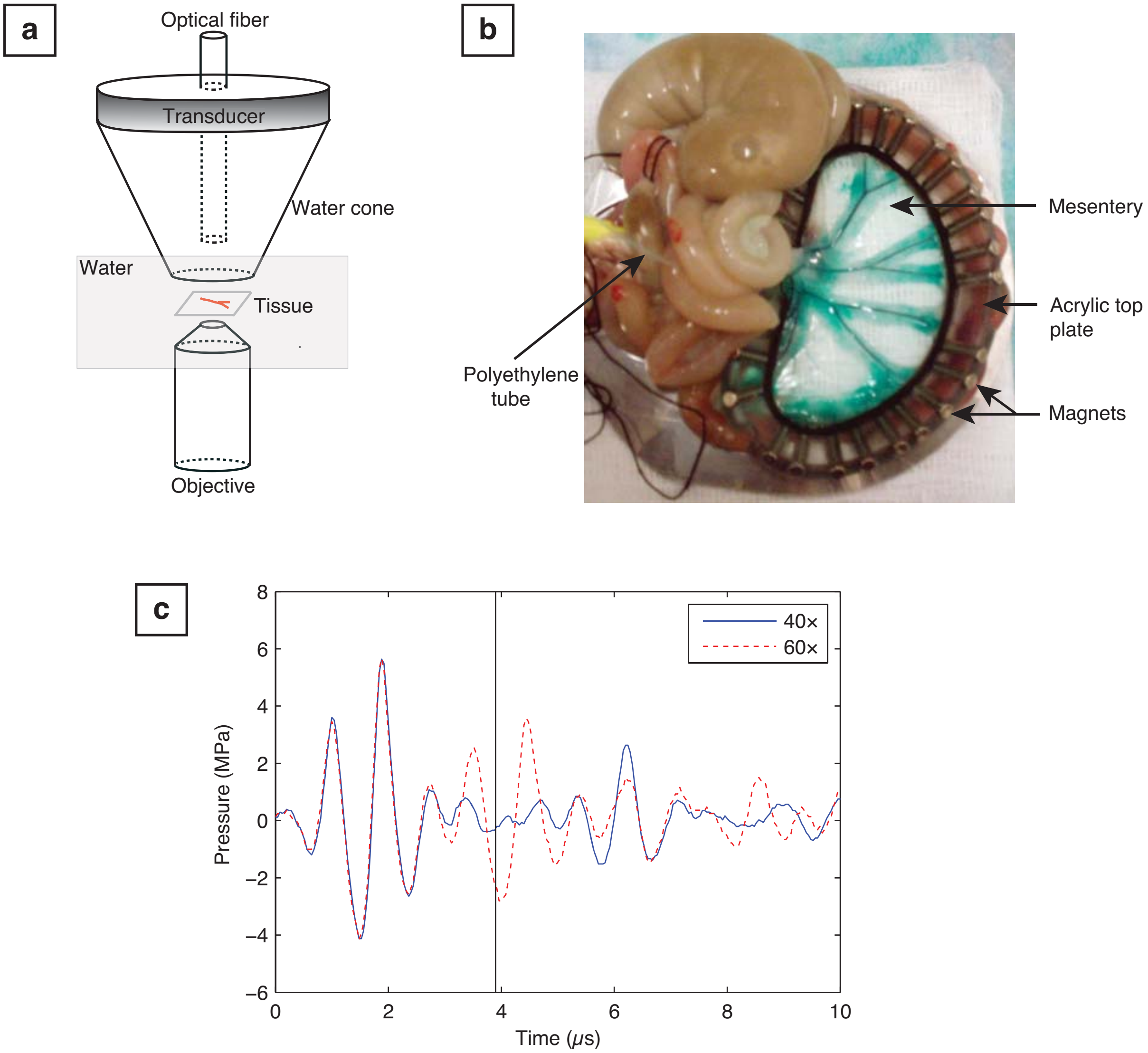

Fig. S1 Arrangement of the experimental setup. (**a**) Illustration of the orientation of the tissue sample relative to the acoustic source and the microscope objective. (**b**) Photograph of excised mesentery tissue held loosely around its periphery by a D-shaped tissue holder. The open central part of the holder was semicircular with a 3.5 cm radius. Around the periphery, an acrylic top plate is held against a back plate with embedded magnets, sandwiching the tissue in between. The thin polyethylene tube at left was used to inject saline mixed with green India ink, thereby coloring parts of the vasculature green. (**c**) Sample acoustic signals measured by a fiber optic hydrophone at the tissue location for both a 40× or 60× objective. High-speed images were captured during the primary acoustic excitation between 0 and 3.9 μs, which is marked by the vertical line. Note that the reflected wave arrives at the target location after images were captured for the 40× objective; however, the reflected wave overlapped with part of the image acquisition for the 60× objective.

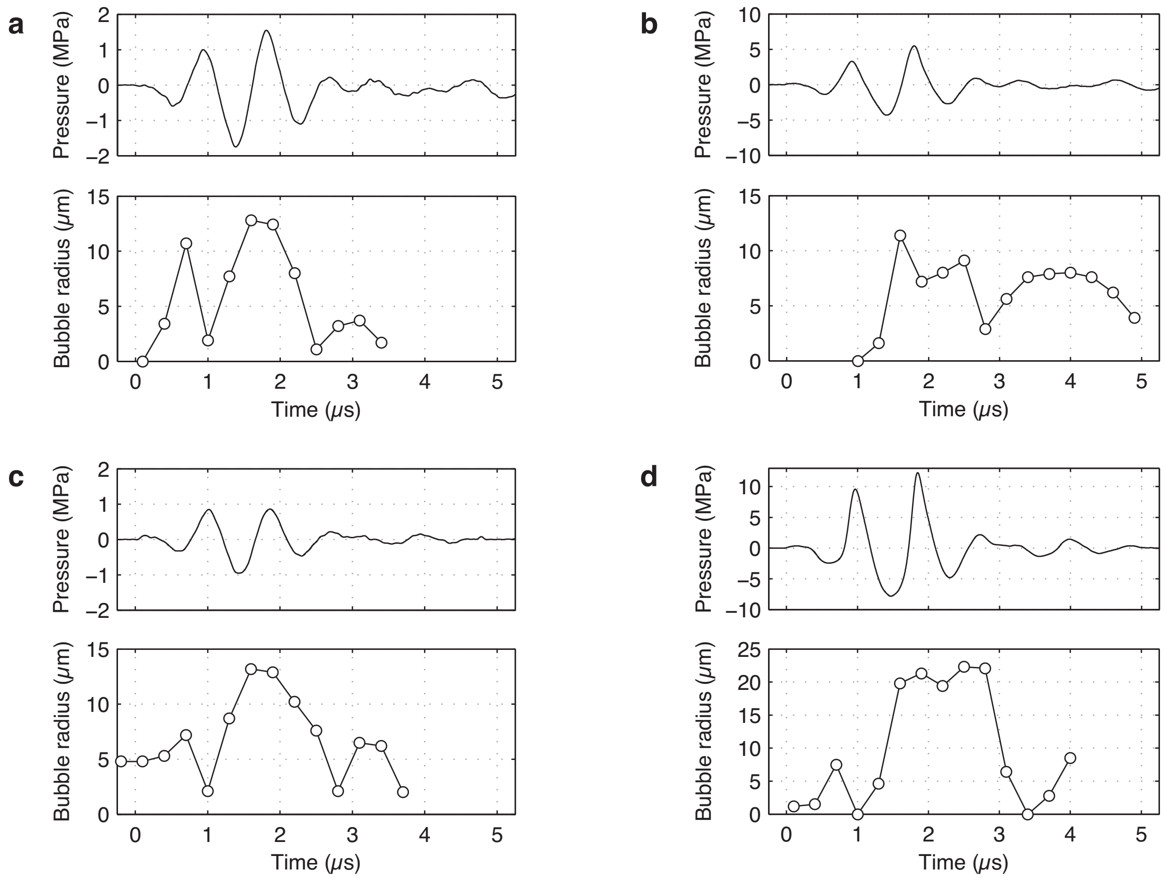

Fig. S2 Pressure waveforms and observed bubble radii for the corresponding photographic sequences from Fig. 2. Pressure waveforms were measured using a fiber optic hydrophone under free-field conditions. Each plotted radius represents the radius of a single spherical bubble with the same volume as observed in a given image frame. Volumes were estimated by assuming ellipsoidal bubble shapes. In (**a**) and (**c**), single bubbles grew and collapsed to roughly track the incident ultrasound pulse. In (**b**), after passage of the incident pressure pulse, the bubble appears to have grown and collapsed again. We speculate that this behavior may have been caused by an interaction with a second bubble that was cropped out of the displayed field of view. In (**d**), the presence of two coalescing bubbles was accounted for by considering the combined volume of both bubbles and calculating an equivalent single-bubble radius.

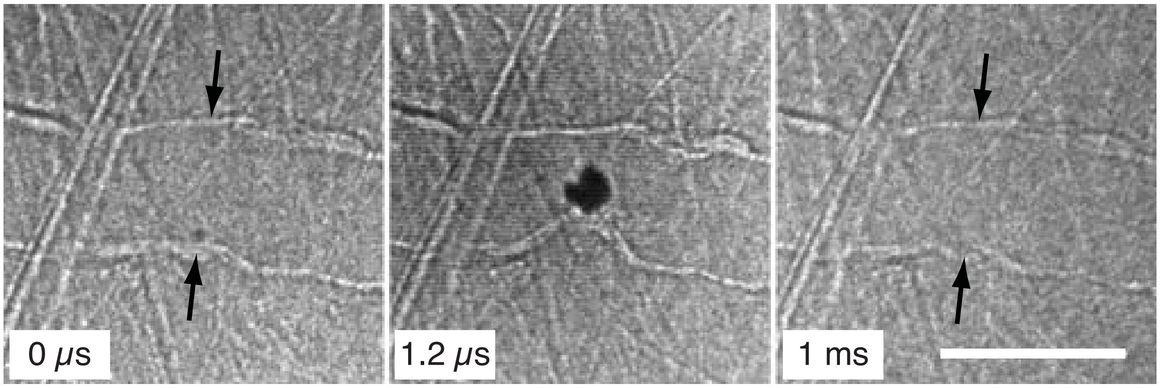

Fig. S3 Three frames from a high-speed photographic sequence to show millisecond relaxation of vessel deformations. Time stamps indicate the time of each frame relative to the arrival of a 2 μs pulse at time zero. The scale bar represents 50 μm. The left frame shows the initial vessel state with the bubble barely visible against the lower vessel wall. The middle frame shows an 11 μm invagination of the lower wall, which is induced by motion of the excited bubble. The right frame depicts the relaxed state of the vessel 1 ms later. To aid the visual comparison, the arrow pairs in the left and right frames are identically spaced. It is clear that after 1 ms, virtually all of the vessel deformation disappeared as the vessel recovered its initial state. Although very slight changes in the apparent shape of the wall are visible, drawing conclusions at this level of detail is diffucult because of the sub-micron depth of field in the images; accordingly, small shifts in the vessel's relative position may alter its appearance. Moreover, additional vessel relaxation may occur over longer durations.

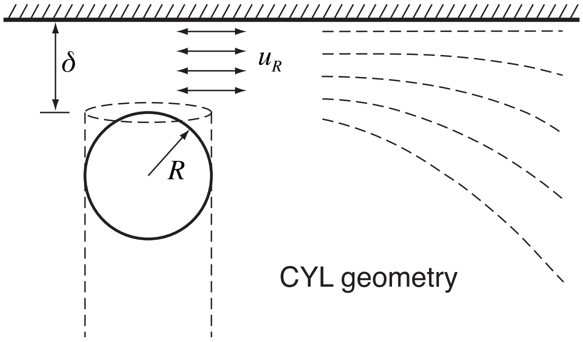

Fig. S4 Schematic of model geometry for flow confinement. A planar boundary alters the geometry of the flow, which is assumed to remain locally cylindrical (CYL) between the bubble and boundary. A spherical bubble of radius R is separated from the boundary by a distance δ. While R and δ vary with time, their sum is assumed to be constant so that the center of the bubble does not translate. The dashed cylinder defines the orientation of a cylindrical coordinate system. The model assumes a purely radial velocity u_R in the gap δ, along with spherically diverging flow as the radial distance from the bubble increases (as indicated by the dashed streamlines sketched on the right).

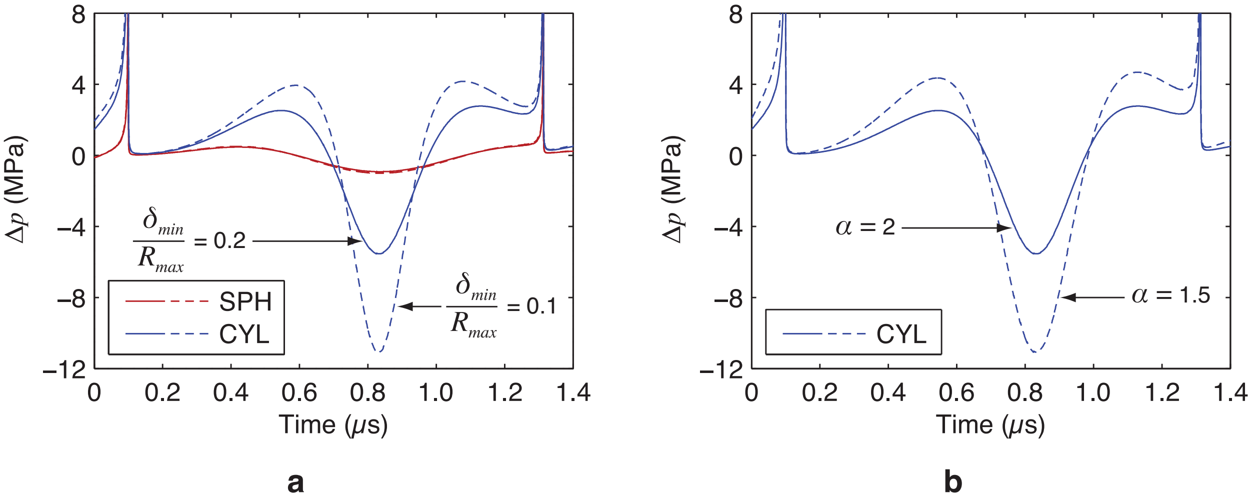

Fig. S5 Simulation of the effects of flow confinement on the pressures generated at a boundary near an oscillating bubble. Simulations considered both spherical (SPH) and locally cylindrical (CYL) flow geometries for a 1 μm bubble excited by a 0.9 MPa sine wave at 1 MHz. To generically simulate inertial bubble motions, radial dynamics were calculated using a Gilmore model for a spherical, adiabatic gas bubble [12]. The sharp, positive pressure spikes in both plots are associated with inertial bubble collapses, while the pressures between spikes vary on a microsecond time scale. Because vessels responded on microsecond time scales (see Fig. 4), we focus on the pressures between spikes. (**a**) Plot demonstrating near-field confinement effects. Defining the standoff distance between the bubble and the boundary in terms of the maximum bubble radius R_{max} and minimum gap δ_{min}, solid lines represent $\delta_{min} = 0.2R_{max}$, while dashed lines represent $\delta_{min} = 0.1R_{max}$. Standoff distance affects pressures very little for a fully spherical flow field (solid and dashed red lines, where the dashed line is mostly hidden by the solid line). However, for locally cylindrical flow that accounts for confinement (solid and dashed blue lines), the magnitudes of both positive and negative pressures increase significantly as δ_{min} decreases; moreover, Δp becomes more negatively biased. (**b**) Plot showing the impact of far-field confinement as described by flow divergence away from the bubble. With the standoff distance fixed ($\delta_{min} = 0.2R_{max}$), the solid line represents the default condition of spherical divergence ($\alpha = 2$), while the dashed line represents a more confined condition ($\alpha = 1.5$). Note that α is defined in Eq. (S7). The additional confinement corresponding to $\alpha = 1.5$ increases pressure magnitudes as well as the negative bias. This concept of far-field confinement can be applied to a bubble in a vessel, though such a geometry is not explicitly modeled here. In particular, for a bubble that grows to fill the vessel cross section, flow streamlines remain virtually parallel to the axis of the vessel and α approaches zero.

Supplementary References

1. Caskey, C. F., Stieger, S. M., Qin, S., Dayton, P. A. & Ferrara, K. W. Direct observations of ultrasound microbubble contrast agent interaction with the microvessel wall. *J. Acoust. Soc. Am.* **122**, 1191–1200 (2007).

2. Freund, J. B. Suppression of shocked-bubble expansion due to tissue confinement with application to shock-wave lithotripsy. *J. Acoust. Soc. Am.* **123**, 2867–2874 (2008).

3. Kundu, P. K. & Cohen, I. M. *Fluid Mechanics* (Academic Press, San Diego, 2002), second edn.

4. Popinet, S. & Zaleski, S. Bubble collapse near a solid boundary: a numerical study of the influence of viscosity. *J. Fluid Mech.* **464**, 137–163 (2002).

5. Brown, M. *Fundamental Neuroscience*, chap. Audition (Elsevier, New York, 2003), 2^{nd} edn.

6. Dumitru, D., King, J. & Zwarts, M. Determinants of motor unit action potential duration. *Clin. Neurophysiol.* **110**, 1876–1882 (1999).

7. Hagiwara, S., Chichibu, S. & Simpson, N. Neuromuscular mechanisms of wing beat in humming birds. *Z. Vgl. Physiol.* **60**, 209–218 (1968).

8. Molloy, J., Kyrtatas, V., Sparrow, J. & White, D. Kinetics of flight muscles from insects with different wingbeat frequencies. *Nature* **328**, 449–451 (1987).

9. Scherer, C. W. *University of Florida Book of Insect Records*, chap. 9, Fastest wing beat, 19–20 (web, accessed Oct. 1, 2009). URL `http://entnemdept.ufl.edu/walker/ufbir/index.shtml`.

10. Patek, S. N., Baio, J. E., Fisher, B. L. & Suarez, A. V. Multifunctionality and mechanical origins: ballistic jaw propulsion in trap-jaw ants. *Proc. Natl. Acad. Sci. U. S. A.* **103**, 12787–12792 (2006).

11. Stryer, L. *Biochemistry* (W. H. Freeman and Company, San Franscisco, 1981), 2^{nd} edn.

12. Leighton, T. G. *The Acoustic Bubble* (Academic Press, San Diego, 1994).

13. Kreider, W., Chen, H., Bailey, M. R., Brayman, A. A. & Matula, T. J. Potential mechanisms for vessel invagination caused by bubble oscillations. In *Proceedings of the IEEE International Ultrasonics Symposium, Rome, Italy, 20–23 Sept. 2009*, 353–356 (2009). [as of 9/13/2010, incorrect revision published online by IEEE].

14. Brujan, E., Nahen, K., Schmidt, P. & Vogel, A. Dynamics of laser-induced cavitation bubbles near an elastic boundary. *J. Fluid Mech.* **433**, 251–281 (2001).

15. Blake, J. R. & Gibson, D. C. Cavitation bubbles near boundaries. *Annu. Rev. Fluid Mech.* **19**, 99–123 (1987).